RMP Colloquia

This section, offered as an experiment beginning in January 1992, contains short articles intended to describe recent research of interest to a broad audience of physicists. It will concentrate on research at the frontiers of physics, especially on concepts able to link many different subfields of physics. Responsibility for its contents and readability rests with the Advisory Committee on Colloquia, U. Fano, chair, Robert Cahn, S. Freedman, P. Parker, C. J. Pethick, and D. L. Stein. Prospective authors are encouraged to communicate with Professor Fano or one of the members of this committee.

Magnetic resonance force microscopy

J. A. Sidles

Department of Orthopaedics, School of Medicine, University of Washington, Seattle, Washington 98195

J. L. Garbini and K. J. Bruland

Department of Mechanical Engineering, University of Washington, Seattle, Washington 98195

D. Rugar, O. Züger, S. Hoen, and C. S. Yannoni

IBM Research Division, Almaden Research Center, 650 Harry Road, San Jose, California 9512C

Recent initial experiments in magnetic resonance force microscopy (MRFM) have detected the magnetic force exerted by electrons and nuclei in microscopic samples. The experiments generate a force signal by modulating the sample magnetization with standard magnetic resonance techniques. Sample sizes of a few nanograms generate readily detected force signals of order 10^{-14} to 10^{-16} Newtons. This article describes the present status of MRFM technology, with particular attention to the feasibility of detecting single-electron magnetic moments, and the possible applications of MRFM in biological imaging.

CONTENTS

I. Introduction 249
II. Determining Molecular Structure in Biology 250
A. Limits of x-ray crystallography and NMR spectroscopy 250
B. Limits of scanning probe microscopy 251
C. Limits of electron microscopy 251
D. The technical challenge of structure determination 251
III. Experiments in MRFM 252
A. Electron spin resonance experiments 252
B. Imaging by MRFM 253
C. Nuclear spin resonance experiments 253
IV. Design Principles in MRFM 253
A. Comparison with inductive detection methods 253
B. Cantilever design parameters 254
C. Noise spectral densities 255
1. Force-noise spectral density 255
2. Other noise spectral densities 255
D. Interferometric noise temperature 256
V. Improving MRFM Sensitivity 257
A. Cantilever relaxation mechanisms 257
B. Fabricating ultrasmall cantilevers 257
VI. MRFM Experiments 257
A. SQUID-based detection of single electrons 258
B. MRFM-based detection of single electrons 260
1. The MRFM field source 260
2. Cantilever design and operation 260
VII. MRFM as a Quantum-Limited Sensing Technology 261
VIII. Stern-Gerlach Effects in Single-Spin Detection 261
IX. MRFM Applications in Magnetism 262
X. Biomolecular Applications of Single-Spin MRFM 262
XI. Conclusion 263
Acknowledgments 263
References 263

I. INTRODUCTION

Recent experiments at IBM have demonstrated the detection and imaging of magnetic resonance signals by the new method of magnetic resonance force microscopy (MRFM) (Rugar, Yannoni, and Sidles, 1992; Züger and Rugar, 1993, 1994; Rugar *et al.*, 1994; Yannoni *et al.*, 1994). In these experiments a microscale force microscope cantilever detects the magnetic force exerted by electron or nuclear magnetic moments in the sample. The sample magnetization is modulated at the resonant frequency of the cantilever by standard magnetic resonance techniques.

Magnetic resonance force microscopy was originally proposed as a means of obtaining three-dimensional images of individual biological molecules, *in situ*, with angstrom resolution (Sidles, 1991; Sidles, Garbini, and Drobny, 1992). MRFM could also have important technological applications, such as imaging subsurface defects in solids and mapping dopant distributions in semiconductors.

 0034-6861/95/67(1)/249(17)/$09.55

This article describes the present status of MRFM research, with particular attention to: (1) the practical limits of present methods for determining molecular structure, (2) the physics and engineering principles of magnetic resonance force microscopy, and (3) the feasibility of detecting individual electron and nuclear magnetic moments.

II. DETERMINING MOLECULAR STRUCTURE IN BIOLOGY

Structural biology is enjoying an epoch of extraordinary vitality. Complete genome sequences of eukaryotic organisms are being compiled with the aid of powerful new laboratory techniques such as the polymerase chain reaction (PCR). Immunohistochemical staining techniques now allow the direct imaging by light microscopy of the distribution of protein species within cells. Many of the biochemical pathways governing cell metabolism have been elucidated, at least in broad outline. Experimental techniques for determining the structure of biological molecules by x-ray crystallography and magnetic resonance are steadily improving.[1]

As new molecular structures are determined, they provide crucial unifying links among existing genomic knowledge, histologic knowledge, and metabolic knowledge. This interplay is illustrated by the recently obtained structure of the human tumor suppressor protein p53 (Friend, 1994), as determined by x-ray crystallography (Cho *et al.*, 1994) and nuclear magnetic resonance (Clore *et al.*, 1994).

p53 is a DNA-binding protein, known to play a fundamental role in regulating human cell growth and differentiation. Approximately half of all human cancer patients carry a p53 mutation (Harris, 1994).

The newly determined p53 structure yielded immediate insight into the mechanism by which p53 regulates cell metabolism:

> The majority of tumorigenic mutations occur in the portion of the core domain structure involved in DNA binding... . A set of mutations appears to eliminate critical DNA contacts, while others appear to destabilize the two loops and the loop-sheet-helix motif involved in DNA binding. The structure thus suggests possible targets for the design of compounds to restore activity to mutant p53 proteins found in tumors (Cho *et al.*, 1994).

New molecular structures suggest unifying links among many previous studies and are greeted with enthusiasm, as noted in a recent review by Friend (1994):

> The parable of the cave in Plato's Republic describes prisoners who are quite satisfied that the shadows on the wall define reality—until the bonds are cut and they view the actual objects. A similar feeling of revelation comes from viewing the three-dimensional structure of the tumor suppressor protein p53, as presented by the crystal structure of the p53 core domain and the solution structure of its oligopolymerization domain.

Typically structure is among the *last* attributes of a biological molecule to be studied; other attributes such as genetic sequence, histological localization, and physiological function are more easily studied, and therefore are determined first.

A. Limits of x-ray crystallography and NMR spectroscopy

In view of successes like the determination of p53's structure, it is tempting to regard molecular structure determination as a solved technical problem. But in fact, present structure determination methods have severe practical limitations. The desire to overcome these limitations motivated early theoretical work in MRFM (Sidles, 1991; Sidles, Garbini, and Drobny, 1992).

X-ray crystallography and nuclear magnetic resonance (NMR) spectroscopy require homogeneous samples, consisting of highly purified solutions or well-ordered crystals. This is a stringent requirement; months or even years of effort may be required to isolate and purify a given molecule before attempting a structure determination. Many obstacles can arise: often the required purification cannot be readily attained, or the molecules are inconveniently large, or the molecules crystallize in a disordered manner.

In such cases the three-dimensional molecular structure cannot readily be determined by *any* present technology. For this reason the great majority of proteins whose sequence is known have unknown structure.[2]

[1] Texts such as Darnell, Lodish, and Baltimore (1990) and Alberts *et al.* (1994) provide a concise summary of modern cell biology. Alberts *et al.* include a useful overview of instrumentation, and the accompanying book of problem sets (Wilson and Hunt, 1994) constitutes a comprehensive and engaging survey of research methods in contemporary molecular biology.

[2] As of January 1994, the Brookhaven Protein Data Bank (Bernstein *et al.*, 1977) contained 1777 entries, comprising 519 differently named molecules. This is only a minute fraction of the 100 000 proteins coded in the human genome, and the hundreds of millions of proteins extant in the biosphere. For example, the HIV-1 genome contains nine genes which produce at least 17 functional proteins (Morrow, Part, and Wakefield, 1994). Yet the Data Bank contains structures of only four HIV proteins, and relatively little is known about the structural interactions of even these four proteins within the cellular environment. It is not for lack of interest that the remaining HIV proteins are absent from the Data Bank, it is rather that no ready means exists to determine their structure.

B. Limits of scanning probe microscopy

To study inhomogeneous biological structures *in situ* with Angstrom-scale spatial resolution, we must turn our attention to imaging technologies.

Direct imaging of atomic-scale structures is accessible to scanning tunneling microscopy (STM) (Binnig *et al.*, 1982a, 1982b, 1983) and atomic force microscopy (AFM) (Binnig, Quate, and Gerber, 1986; Gould *et al.*, 1990; Rugar and Hansma, 1990). Relative to x-ray crystallography and NMR spectroscopy, STM and AFM techniques have the great advantage of directly imaging inhomogeneous samples. There has been significant progress in recent years in the STM and AFM imaging of DNA (Driscoll, Youngquist, and Baldeschwieler, 1990; Amrein *et al.*, 1989; Youngquist *et al.*, 1991; Hansma *et al.*, 1991, 1993; Mastrangelo *et al.*, 1994), as well as proteins and other biomolecules (Drake *et al.*, 1989; Weisenhorn *et al.*, 1990; Rees *et al.*, 1993; Lal and John, 1994). However, sequencing of DNA and proteins by STM or AFM has not yet been achieved.

STM and AFM devices act primarily on the topmost layer of atoms, via conduction band and Coulomb interactions. Often the topmost layer of atoms is precisely the region of greatest scientific interest, for example, in surface science, where STM and AFM have had a revolutionary scientific impact. However, the features of greatest interest in structural biology are three-dimensional binding sites. These typically occur within narrow clefts, beyond the reach of conventional AFM and STM tips.

C. Limits of electron microscopy

Electron microscopy is by far the most widely used and generally applicable technique for imaging inhomogeneous biological structures with submicron spatial resolution.

The freeze-fracture image of Fig. 1 offers a tantalizing glimpse of the intricate *in situ* molecular structure that exists within every eukaryotic cell.[3] The illustrated surface contains roughly 10 000 protein molecules, immobilized *in situ* by the cryogenic temperatures that accompany the freeze-fracture process.[4]

From the perspective of modern structural biology, these proteins constitute an intricate self-replicating mechanism whose structure remains largely unknown.

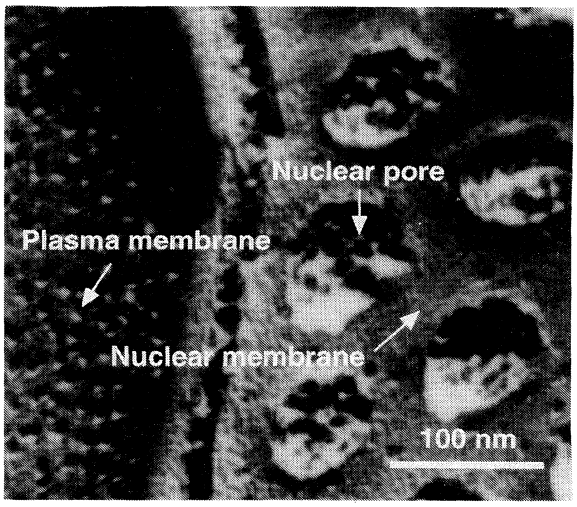

FIG. 1. Electron microscope image of a mouse sperm cell. The larger "domes" are nuclear pore structures embedded in the nuclear membrane. Tightly packed nanometer-scale particles in the plasma membrane also are featured. The detailed molecular structure of these features is unknown, and cannot readily be determined by any existing technology.

Figure 1 was obtained by rapidly freezing a sperm cell, fracturing it along a nuclear membrane, shadowing the fractured surface with a 20-Å-thick coating of platinum, and imaging the resulting replica under a transmission electron microscope.[5] The metal replica yields the primary image; proteins themselves are composed almost entirely of light elements which are relatively transparent to electron beams. The resulting spatial resolution falls far short of the three-dimensional detail provided by x-ray crystallography.

For this reason, it is widely appreciated by practicing biologists that (Alberts *et al.*, 1994)

> Regardless of the method used, a single protein molecule gives only a weak and ill-defined image in the electron microscope... . Problems of specimen preparation, contrast, and radiation damage effectively limit the normal resolution for biological objects to 20 Å.

D. The technical challenge of structure determination

It is natural to ask whether there exists *any* practical means, even in principle, of directly imaging biomolecular structures *in situ*. This question constitutes a well-

[3]Roberts, Kessel, and Tung (1991) have published an atlas of freeze-fracture images encompassing many human cell types. Their images illustrate the diversity of nanometer-scale structure present in living tissues. The atlas also provides an up-to-date description of freeze-fracture preparation techniques.

[4]The freeze-fracture process presumably alters the tertiary structure of proteins to some extent. However, cryocrystallography studies of frozen crystal specimens show minimal disruption of tertiary protein structure (Bartunik *et al.*, 1992), and this observation is consistent with the commonplace medical and veterinary practice of freezing and thawing mammalian embryos without loss of vitality.

[5]Our thanks to Professor James K. Koehler of the University of Washington Department of Biological Structure for providing this micrograph.

defined and medically important scientific challenge. As noted by Stuart (1994),

> For every biological problem that has succumbed to structural analysis, there are many more that have kept their secrets. Often we tactfully gloss over these and turn to easier, if less significant questions.

This limitation is readily apparent to researchers in clinical medicine. Structural hypotheses that are clinically important, but difficult or impossible to investigate with existing technologies, cannot (and should not) compete effectively for funding with more feasible proposals. But as the literature on HIV infection attests, the scientific community can publish a great number of research articles on a given topic, yet still not attain a reliable understanding of even the most basic mechanisms of pathogenesis.

The lack of comprehensive technologies for structure determination is arguably one of the main limitations preventing a more satisfactory rate of progress.

Magnetic resonance force microscopy was conceived as the result of a systematic theoretical search for a molecular imaging technology that would address the practical needs of biological researchers by being (1) nondestructive, (2) three-dimensional, (3) capable of Angstrom-scale spatial resolution, and (4) able to image individual biological molecules *in situ*.

Whether these goals can be achieved, even in principle, is an issue that deserves to be carefully considered by the physics and engineering community. Obviously MRFM is not the only technique that might be considered.

To achieve nondestructive three-dimensional imaging, MRFM adopts from magnetic resonance imaging the concept of selectively exciting magnetic resonance within a "slice" of a sample (Lauterbur, 1973; Mansfield and Morris, 1982). The elemental and isotopic selectivity of magnetic resonance is an added bonus.

To achieve Angstrom-scale spatial resolution, MRFM combines aspects of scanning tunneling microscopy (Binnig *et al.*, 1982a, 1982b, 1983) and scanning force microscopy (Binnig, Quate, and Gerber, 1986). In particular, the technical feasibility of generating and controlling three-dimensional scanning motions with Angstrom-scale accuracy was first demonstrated by these technologies.

To achieve the required magnetic-moment sensitivity, MRFM includes aspects of magnetic force microscopy (Martin and Wickramasinghe, 1987; Sáenz *et al.*, 1987; Hobbs, Abraham, and Wickramasinghe, 1989; Mamin *et al.*, 1989; Albrecht *et al.*, 1991).

III. EXPERIMENTS IN MRFM

To date, all MRFM experiments have operated in a similar manner, as illustrated in Fig. 2 (Rugar, Yannoni, and Sidles, 1992; Züger and Rugar, 1993, 1994; Rugar *et al.*, 1994; Yannoni *et al.*, 1994). A sample to be observed by magnetic resonance is affixed to a force microscope cantilever, and a permanent magnet is placed nearby. The magnetic field gradient then exerts a force on the cantilever. The force derives either from unpaired electron spins in the sample, or from nuclear magnetic moments. A nearby radio-frequency coil modulates the sample magnetization at the resonant frequency of the cantilever, by any of the large number of techniques that have been described in the magnetic resonance literature (Abragam, 1961; Slichter, 1989). The resulting excitation of the cantilever is sensed by optical-fiber interferometry.

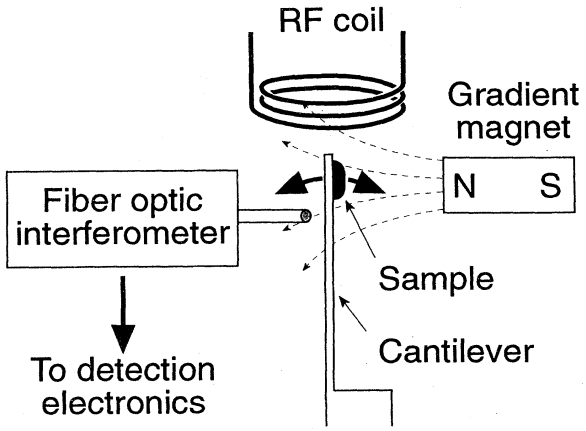

FIG. 2. A representative MRFM experiment.

A. Electron spin resonance experiments

The first MRFM experiment was performed at IBM Almaden Research Center by a team led by Dan Rugar (Rugar, Yannoni, and Sidles, 1992). This experiment

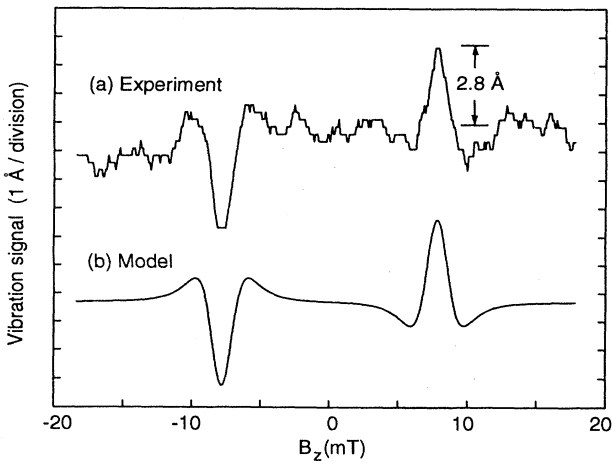

FIG. 3. MRFM experimental data vs theoretical prediction, for detection of electron spin resonance in DPPH (from Rugar, Yannoni, and Sidles, 1992). Here B_z is the polarizing field strength.

detected electron spin resonance in a 30-ng sample of the paramagnetic substance diphenylpicrylhydrazil (DPPH).

The sample magnetization was modulated by the method of cyclic saturation (Garstens and Kaplan, 1955; Whitfield and Redfield, 1957). The detected force was 10^{-14} N, and the measured signal and noise were in good agreement with theoretical predictions (Fig. 3).

B. Imaging by MRFM

Soon after the initial detection of magnetic resonance by MRFM, Züger and Rugar (1993, 1994) demonstrated image reconstructions. The force microscope apparatus was as shown in Fig. 2, and the magnetic tip was raster scanned over a paramagnetic sample of DPPH.

Figure 4 shows the first images obtained by MRFM. The image resolution was 5 μm laterally and 1 μm axially (Züger and Rugar, 1993, 1994). The images were deconvolved from raw data by a Wiener filtering technique.

The slice-selective nature of the MRFM tip-sample interaction facilitates image reconstruction. In conventional force microscopy, the tip-sample interaction increases in strength as the tip moves closer to the sample. But in MRFM experiments the strongest interaction involves spins located at a determinate distance from the tip, where the spin precession frequency resonates with the applied RF field (Fig. 5). Similar slice selectivity is an essential element of medical magnetic resonance imaging.

C. Nuclear spin resonance experiments

MRFM detection of nuclear magnetism in a sample size of a few nanograms has recently been demonstrated (Rugar *et al.*, 1994), by means of a 900-Å-thick silicon nitride cantilever having a force sensitivity of 5×10^{-16} N/$\sqrt{\text{Hz}}$ at room temperature (Fig. 6). The sample magnetization was modulated by cyclic adiabatic inversion of proton spins (Abragam, 1961).

The experiment achieved a single-shot NMR sensitivity

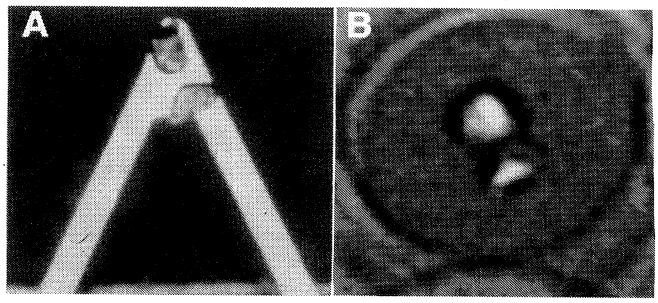

FIG. 4. Imaging by MRFM. (a) Optical micrograph showing two DPPH particles (20 μm wide) attached to a silicon nitride cantilever. (b) The reconstructed image, with the two DPPH particles appearing as two bright features. The large rings slightly visible in the image are artifacts of the deconvolution procedure (from Züger and Rugar, 1994).

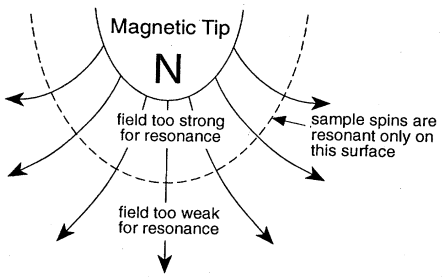

FIG. 5. The resonant tip-sample interaction in MRFM.

of 1.6×10^{13} protons at room temperature. The spatial resolution was 2.6 μm, an order of magnitude better than that obtained by conventional NMR imaging of solids.[6]

IV. DESIGN PRINCIPLES IN MRFM

The following aspects of MRFM distinguish it from conventional scanning force and tunneling microscopy:

(1) The magnetic imaging interaction is noncontact and specific to electron and nuclear spins.

(2) The imaging magnetic field is three-dimensional and reaches below the scanned surface, as is desirable for imaging subsurface structures.

(3) The theory of magnetic resonance provides a reliable basis for predicting signal characteristics, and the resulting image deconvolution algorithms are numerically well-conditioned.

But there is a price to be paid for these advantages: MRFM signals carry little energy, just as in conventional magnetic resonance imaging. Magnetic resonance imaging is nondestructive precisely *because* the signal quanta are low energy. In contrast, imaging with energetic quanta like electrons or x rays makes signal detection relatively easy, but also entails an increased likelihood of specimen damage.

A. Comparison with inductive detection methods

Sidles and Rugar (1993) have compared the sensitivity of MRFM to that of conventional inductive magnetic resonance detection.

MRFM and inductive detection both involve the magnetic coupling of a sample to an oscillator. In MRFM the oscillator is a mechanical cantilever, coupled to the sample by a magnetic force. In coil-based detection the oscillator is a tuned inductor-capacitor pickup coil, coupled to the sample by a magnetic flux (Fig. 7).

[6]For a review of solid-state NMR imaging, see Cory (1992).

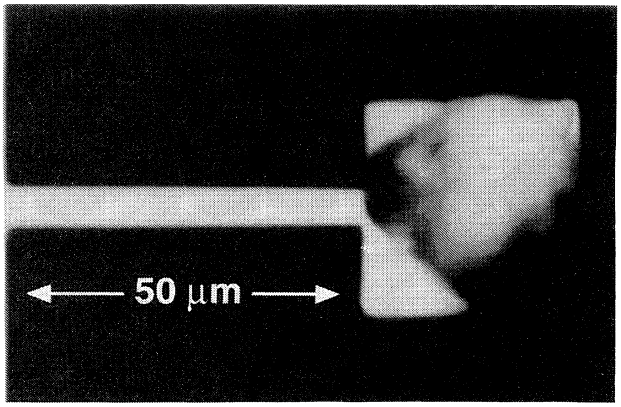

FIG. 6. Optical micrograph of a 900-Å thick silicon nitride cantilever. A small grain of the sample material (ammonium nitrate) is visible on the upper portion of the paddle-shaped cantilever tip. The narrow neck of the cantilever is 50 μm long and 5 μm wide (from Rugar *et al.*, 1994).

Sidles and Rugar (1993) show that three parameters suffice to characterize both types of detection. Two of the parameters are familiar: the oscillator resonant frequency ω_0 and the quality factor Q. The third parameter is a magnetic stiffness $k_{\rm mag}$ defined as follows. Both mechanical and electrical oscillators create an oscillating magnetic field amplitude $B(t)$ at the sample. In a Hamiltonian formalism the required energy appears as a potential energy term

$$(\text{potential energy}) = k_{\rm mag} B^2/2, \tag{4.1}$$

which implicitly defines the magnetic stiffness $k_{\rm mag}$. Physically, small values of $k_{\rm mag}$ mean that an oscillator requires little energy to generate an oscillating magnetic field.

Thermal noise in the oscillator is dynamically equivalent to the noise created by a fluctuating sample magnetic moment μ with spectral density S_μ at a temperature T:

$$S_\mu = \frac{k_{\rm mag}}{Q\omega_0}\, 4k_B T. \tag{4.2}$$

Here ω_0 is expressed in radians/second (not Hz), and k_B represents Boltzman's constant.[7] Thus the mean-square magnetic-moment noise $\langle \mu^2 \rangle$ in a bandwidth b (in Hz) is $\langle \mu^2 \rangle = S_\mu b$.

The magnetic stiffness of a receiver coil depends mainly on the coil volume $V_{\rm coil}$, and is reasonably independent of the number of coil windings and of the coil aspect ratio:

[7]The bandwidth normalization convention for S_μ and all other spectral densities in this article is that bandwidths are specified in Hz and encompass only positive frequencies. Most engineering texts and spectral analyzers employ this convention. The numerical factor "4" in Eq. (4.2) has the same mathematical origin and physical interpretation as the "4" in the familiar expression for the spectral density S_V of Johnson voltage noise in a resistance R: $S_V = 4\,k_B T\,R$.

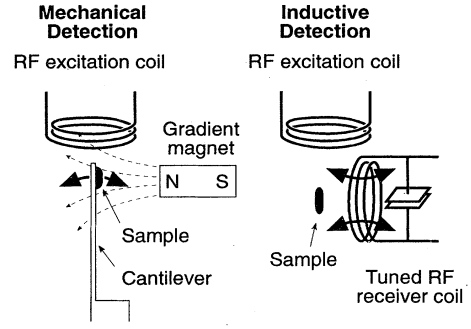

FIG. 7. Mechanical vs inductive detection of magnetic resonance.

$$k_{\rm mag} \simeq 2V_{\rm coil}/\mu_0 \quad \text{(SI units)}$$
$$= V_{\rm coil}/2\pi \quad \text{(Gaussian units)}. \tag{4.3}$$

In a mechanical cantilever, $k_{\rm mag}$ is related to the mechanical spring constant $k_{\rm mech}$ by

$$k_{\rm mag} = k_{\rm mech}/g^2, \tag{4.4}$$

where g represents the local magnetic field gradient generated by the MRFM device.

Physically speaking, an inductive coil creates and then annihilates its magnetic field twice during each cycle, entailing an energy cost proportional to the coil volume. A mechanical oscillator avoids this energy cost by a trick; rather than the field being annihilated, the sample (or alternatively, the field source) is moved to another location. This exchanges one energy cost for another: the sample (or field source) still must be vibrated back and forth, which entails the expenditure and storage of kinetic energy. Smaller cantilevers are easier to move, thus microscale cantilevers can serve as exceptionally sensitive detectors.

The motional mass of the cantilever in Fig. 4 is only 40 ng. Assuming a signal amplitude of ~ 1 Å at ~ 8 kHz (which is a readily observable signal), the cantilever velocity is only 2 cm/hr. The resulting excitation energy is only $\sim 10^{-21}$ Joules, allowing the first MRFM experiment to achieve a magnetic-moment sensitivity comparable to the best available room temperature inductive coils.

B. Cantilever design parameters

Figure 8 depicts a clamped cantilever beam of length l, width w, and thickness t. For a cantilever material of density ρ and Young's modulus E, the resonant frequency ω_0 of the lowest-order flexural mode is

$$\omega_0 = 3.516\,\frac{t}{l^2}\left(\frac{E}{12\rho}\right)^{1/2} \tag{4.5}$$

(Morse, 1936; Mason, 1942). The dimensionless factor

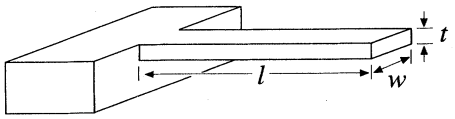

FIG. 8. Cantilever geometry.

3.516 is a modal eigenvalue.

The effective spring constant $k_{\rm mech}$ as measured at the cantilever tip is

$$k_{\rm mech} = m_{\rm eff}\,\omega_0^2 \tag{4.6}$$

$$= 1.030\,\frac{1}{4}\,\frac{Ewt^3}{l^3}. \tag{4.7}$$

Here $m_{\rm eff} = \rho lwt/4$ is the motional mass of the cantilever. The factor 1.030 indicates that the fundamental flexural mode is ~3% stiffer than a statically bent beam.

These results are readily generalized to higher-order flexural modes. The eigenfrequencies of the first four flexural modes are

$$\omega_0 = \begin{bmatrix} 3.516 \\ 22.03 \\ 61.70 \\ 120.90 \end{bmatrix} \frac{t}{l^2}\left(\frac{E}{12\rho}\right)^{1/2}. \tag{4.8}$$

The motional mass $m_{\rm eff} = \rho lwt/4$ is the same for all flexural modes of a clamped beam (Morse, 1936). The second mode is 6.3 times higher in frequency than the fundamental mode, so the effective spring constant $k_{\rm mech}$ is $6.3^2 \approx 40$ times greater. Only the fundamental mode has been used in MRFM experiments to date.

Recently Neumeister and Ducker (1994) and Chen *et al.* (1994) have used numerical methods to analyze the modal properties of more complicated cantilever designs. Commercial finite element packages also are suitable for this task. Only Q is not readily susceptible to engineering analysis.

C. Noise spectral densities

1. Force-noise spectral density

Thermal noise in a cantilever is manifested as Brownian motion equivalent to that generated by a Langevin random force $F(t)$ whose spectral density S_F is related to the magnetic-moment spectral density S_μ [Eq. (4.2)] by

$$S_F = g^2 S_\mu$$

$$= \frac{k_{\rm mech}}{Q\omega_0}\,4k_BT, \tag{4.9}$$

with ω_0 expressed in radians/sec. Our bandwidth convention sets the minimum detectable root-mean-square force in a bandwidth b with unit signal-to-noise ratio at $F_{\rm min} = (S_F\,b)^{1/2}$.

We can write $F_{\rm min}$ in three equivalent ways:

$$F_{\rm min} = (4k_BT\,b)^{1/2}\left(\frac{k_{\rm mech}}{Q\omega_0}\right)^{1/2} \tag{4.10a}$$

$$= (4k_BT\,b)^{1/2}\left(\frac{m_{\rm eff}\omega_0}{Q}\right)^{1/2} \tag{4.10b}$$

$$= (4k_BT\,b)^{1/2}\left(\frac{m_{\rm eff}}{\tau}\right)^{1/2}. \tag{4.10c}$$

Here $\tau = Q/\omega_0$ is the damping time.

The simplest design insights are offered by Eq. (4.10c), which contains only the two oscillator parameters $m_{\rm eff}$ and τ. At a fixed oscillator damping time τ, the motional mass $m_{\rm eff}$ should be minimized, while the spring constant $k_{\rm mech}$ and the oscillator frequency ω_0 are immaterial. In this respect neither high-frequency nor low-frequency mechanical oscillators offer an intrinsic advantage in force sensitivity.

2. Other noise spectral densities

Thermal noise in a cantilever may be regarded as arising from many different but fully equivalent effective noise sources. We have obtained expressions for the effective magnetic-moment noise S_μ [Eq. (4.2)] and force noise S_F [Eq. (4.9)]; now we will derive equivalent expressions for torque noise, spring constant noise, and frequency noise.

When the cantilever shown in Fig. 8 vibrates in its fundamental flexural mode, its tip moves with a linear combination of translation q and angular deflection θ according to $\theta = 1.377\,q/l$. The coefficient 1.377 represents the slope of the fundamental mode at the tip of the cantilever. The slope values for the first four flexural modes of a clamped beam are $\{1.377, 4.788, 7.849, 11.996\}$.

In consequence, an oscillating torque with amplitude J, applied to the tip of the cantilever at the resonant frequency of the fundamental mode, is kinematically equivalent to an oscillating force $F = 1.377\,J/l$. Thus an MRFM cantilever can serve as a torque detector, and its Brownian motion may be regarded as arising from a Langevin torque $J(t)$ with spectral density S_J,

$$S_J = (l/1.377)^2\,S_F. \tag{4.11}$$

To describe thermal noise from another useful perspective, suppose we measure the cantilever's resonant frequency ν_0 [in Hz, so that $\nu_0 = \omega_0/(2\pi)$], or equivalently the spring constant $k_{\rm mech} = m_{\rm eff}\omega_0^2$. This may be accomplished by driving the cantilever on-resonance such that its mean-square tip excitation is some convenient value $\langle z^2\rangle$. Changes in $k_{\rm mech}$ alter the phase of the excitation relative to the phase of the driving force, yielding a phase shift that is readily measured with a lock-in amplifier. Thermal noise in the cantilever creates fluctuations in the measured phase; these in turn create fluctuations in the inferred value of $k_{\rm mech}$.

Alternatively, the cantilever may be driven by a gain-controlled feedback circuit, with changes in the resonant frequency measured directly from the feedback signal. Albrecht *et al.* (1991) have shown that this latter method has a detection bandwidth significantly greater than the natural bandwidth of the cantilever, which is an important practical advantage.

Both experimental methods yield the same spectral density S_k of thermal fluctuations in $k_{\rm mech}$

$$S_k = \frac{S_F}{\langle z^2 \rangle} \quad [\text{SI units of } (\text{N/m})^2/\text{Hz}], \tag{4.12}$$

which is equivalent to a spectral density S_ν of thermal fluctuations in ν_0

$$\begin{aligned} S_\nu &= \left(\frac{\nu_0}{2k_{\rm mech}}\right)^2 S_k \\ &= \left(\frac{\nu_0}{2k_{\rm mech}}\right)^2 \frac{S_F}{\langle z^2 \rangle} \quad (\text{SI units of } \text{Hz}^2/\text{Hz}). \end{aligned} \tag{4.13}$$

Seemingly, S_k and S_ν can be made arbitrarily small by setting $\langle z^2 \rangle$ arbitrarily large, but practical considerations such as oscillator nonlinearity limit the feasible drive amplitude.

D. Interferometric noise temperature

To date, all MRFM experiments have detected cantilever excitation by fiber-optic interferometry (Rugar, Mamin, and Guethner, 1989). The following discussion follows the analysis of interferometer noise by Edelstein *et al.* (1978) in the context of gravity-wave detection, as adapted by Rugar and Grütter (1991) in a discussion of cantilever-based force detection.

We adopt the idealizing assumptions that (1) all photons reflected from the cantilever are captured by the interferometer fiber, (2) the reflected photons are detected with unit efficiency, and (3) the interferometer is adjusted to have unit fringe visibility (see Rugar and Grütter, 1991). Then the flux $R_{\rm det}$ of photons arriving at the photodetector (in photons per second) is related to the flux $R_{\rm cant}$ of photons incident on the cantilever by

$$R_{\rm det} = R_{\rm cant}\,[1 - \cos(4\pi d/\lambda)]\,. \tag{4.14}$$

Here $4\pi d/\lambda$ is the interferometer phase, with d the fiber-to-cantilever distance and λ the wavelength of interferometer light. Typically d is adjusted so that $\cos(4\pi d/\lambda) = 0$; this maximizes the sensitivity of the interferometer and we assume it henceforth. Then $R_{\rm det} = R_{\rm cant} \equiv R$.

The spectral density of fluctuations in the photon flux is simply $S_R = 2R$ (the familiar spectral density of shot noise), and each reflected photon transfers momentum $4\pi\hbar/\lambda$ to the cantilever. This creates a fluctuating backaction force whose spectral density $S_F^{\rm back}$ is

$$S_F^{\rm back} = 2R\,(4\pi\hbar/\lambda)^2\,. \tag{4.15}$$

Similarly, a fluctuation δR in the measured photon flux is equivalent to a fluctuation δq in the cantilever tip displacement q according to $\delta q = \delta R\,\lambda/(4\pi R)$. Therefore, shot noise in the interferometer detector is equivalent to displacement fluctuations with spectral density $S_q^{\rm shot} = 2R\,[\lambda/(4\pi R)]^2$. For frequencies within the bandwidth of the cantilever, $S_q^{\rm shot}$ is equivalent to an effective force with spectral density $S_F^{\rm shot}$

$$S_F^{\rm shot} = \left(\frac{k_{\rm mech}}{Q}\right)^2 S_q^{\rm shot} = \frac{2}{R}\left(\frac{k_{\rm mech}}{Q}\right)^2 \left(\frac{\lambda}{4\pi}\right)^2. \tag{4.16}$$

Note that $S_F^{\rm back}$ increases with increasing photon flux R, while $S_F^{\rm shot}$ decreases. These opposing tendencies ensure that there is an optimal photon flux $R_{\rm opt}$, which minimizes $S_F^{\rm shot} + S_F^{\rm back}$:

$$R_{\rm opt} = \frac{k_{\rm mech}}{Q\hbar}\left(\frac{\lambda}{4\pi}\right)^2. \tag{4.17}$$

The corresponding optimal optical power $I_{\rm opt}$ is

$$I_{\rm opt} = \frac{2\pi\hbar c}{\lambda} R_{\rm opt} = \frac{c\lambda k_{\rm mech}}{8\pi Q}, \tag{4.18}$$

where c is the speed of light.

The total noise spectral density $S_F^{\rm tot}$ is the sum of shot noise $S_F^{\rm shot}$, backaction noise $S_F^{\rm back}$, and thermal noise $S_F^{\rm thermal}$ [see Eq. (4.9)]. $S_F^{\rm tot}$ takes an especially simple form when the interferometer is operated at the optimal optical power level $I_{\rm opt}$:

$$\begin{aligned} S_F^{\rm tot} &= S_F^{\rm shot} + S_F^{\rm back} + S_F^{\rm thermal} \\ &= \frac{4k_{\rm mech}}{Q\omega_0}\,(\hbar\omega_0 + k_B T)\,. \end{aligned} \tag{4.19}$$

The noise temperature of an optimized interferometer thus equals precisely one quantum of oscillator energy.[8] The noise temperature is independent of the cantilever parameters ω_0, $k_{\rm mech}$, and Q, provided the optical power is optimized. The noise spectral densities $\{S_\mu, S_F, S_k, S_\nu\}$ share the same noise temperature because they are linearly related.

The ideal interferometer noise temperature of a 10 kHz cantilever (a typical MRFM frequency) is only 0.5 μK. However, real-life interferometers are always nonideal to some extent, because of limited photon detection efficiency, or because some photons reflected by the cantilever are not captured by the fiber, or because the input laser is noisy. Cantilever heating by interferometer

[8] The interferometer noise temperature can be further reduced to $\hbar\omega_0/\sqrt{2}$ by modifying the Michelson interferometer described by Edelstein *et al.* (1978) such that light transmitted back toward the laser source is detected (see Fig. 1 in Edelstein's article) or, alternatively, by operating one interferometer arm near a dark fringe and detecting only the flux in the dark arm. In principle, optical quantum nondemolition techniques may be exploited to achieve even greater sensitivity (Caves, 1980, 1981; Pace, Collett, and Walls, 1993); these have not yet been demonstrated in the context of MRFM.

beam absorption may cause problems at low temperatures. Nonetheless, in all MRFM experiments to date interferometer noise temperatures have been negligibly small compared to ambient temperatures, so that Brownian motion of the cantilever is the dominant noise source.

V. IMPROVING MRFM SENSITIVITY

The previous results imply that the root-mean-square magnetic moment $\mu_{\min}$ detectable in a bandwidth b with unit signal-to-noise ratio is

$$\mu_{\min} = \frac{1}{g}\left(\frac{m_{\text{eff}}}{\tau} 4k_B T\, b\right)^{1/2} (\text{SI units of A m}^2). \quad (5.1)$$

This expression makes it clear that MRFM sensitivity may be systematically improved by fabricating cantilevers with (1) longer damping times and (2) smaller motional mass, then equipping the MRFM device with (3) stronger magnetic gradients and operating it at (4) lower temperatures.

A. Cantilever relaxation mechanisms

All the design parameters of MRFM devices are subject to engineering specification and control *except* cantilever quality Q. Typically Q is determined empirically, by looking at the spectrum of cantilever Brownian motion after the device has been fabricated.

Achieving a reliable understanding of cantilever damping mechanisms is an important issue in MRFM research. There is an abundance of literature on the general subject of acoustic and mechanical relaxation mechanisms. Mason's multivolume *Physical Acoustics* series contains several relevant review articles (Berry and Nowick, 1966; Granato and Lucke, 1966; Klemens, 1966; Mason, 1966; Fraser, 1968), each of which lists many additional references. Blair (1991) similarly reviews the large body of theoretical and experimental literature relating to relaxation mechanisms in macroscale resonant bar detectors (see, particularly, Ferreirinho, 1991).

Relaxation mechanisms of likely relevance to MRFM include mechanical losses associated with gas damping, Rayleigh waves propagating into the substrate from the cantilever base, three-phonon and four-phonon anelastic scattering (possibly in the presence of a nonequilibrium phonon distribution created by optical heating), thermoelastic damping, metallic coating damping, dislocation damping, and surface contaminant damping.

With specific reference to relaxation mechanisms in micromechanical oscillators, Roszhart (1990) has presented an analysis of thermoelastic friction in single-crystal silicon resonators, referencing Zener's pioneering work in the field (Zener, 1937, 1938; Randall, Rose, and Zener, 1939). Langdon and Dowe (1987), Pitcher *et al.* (1990), and Zhang, Uttamchandani, and Culshaw (1990) have investigated optothermal interactions between laser light and silicon cantilevers. Buser and de Rooij (1990) have fabricated high-Q resonators in monocrystalline silicon, achieving Q of 6×10^5 at room temperature, but in a millimeter-scale oscillator that is too massive for MRFM use. Zook *et al.* (1992) have reviewed the mechanical characteristics of polysilicon resonant microbeams.

As yet, no authors have investigated damping mechanisms in oscillators that are optimized for MRFM applications, that is to say, oscillators designed with the lowest possible mass and the longest possible damping time, and operated at the lowest possible temperature. It is not known whether cantilevers provide the optimal design choice for MRFM oscillators. Conceivably torsional mechanical oscillators or shear mode oscillators could offer superior performance.

B. Fabricating ultrasmall cantilevers

Hoen *et al.* (1994) have fabricated amorphous silicon nitride cantilevers specifically for MRFM experiments. These authors recognized that the easiest cantilever dimension to make small is the thickness of the cantilever, which is determined by thin-film deposition, as opposed to optical lithography.

The smallest cantilever described by Hoen *et al.* (1994) is 55 μm long, 5 μm wide, and only 200 Å thick. This cantilever is a thinned version of the cantilever "neck" shown in Fig. 6.

Surprisingly, these microscale cantilevers display mechanical properties resembling those predicted from the bulk properties of silicon nitride, even though they are no thicker than a large protein molecule and have proportions resembling a $1'' \times 11''$ strip of typing paper.

Recently, Binh *et al.* (1994) fabricated submicron-scale tungsten cantilevers, which have predicted resonant frequencies in the GHz range. These cantilevers have not yet been used for force microscopy.

VI. MRFM EXPERIMENTS

In principle, many different experiments in the magnetic resonance literature can be repeated by MRFM. The question then arises: which experiments will achieve a reasonable signal-to-noise ratio? We have endeavored to convey to the reader all the design tools needed to answer this question on a case-by-case basis.

Ferromagnetism, paramagnetism, and nuclear magnetism all exhibit magnetic resonance phenomena. There are at least three means of cyclically modulating sample magnetization: (1) cyclic saturation, (2) cyclic adiabatic inversion, and (3) precession resonance. Of these, cyclic saturation and adiabatic inversion modulate the sample magnetization at frequencies much lower than the spin precession frequency, and thus are well suited to commercial audio-frequency force microscope cantilevers. Precession resonance experiments require higher-frequency cantilevers whose resonance is matched to the spin precession frequency; at present this is only a theoretical

TABLE I. Experiments in MRFM organized by type of magnetization and method of modulation.

Method of modulation	Ferromagnetism	Paramagnetism	Nuclear magnetism
Cyclic saturation	Strong sample magnetization would yield large signal. Would require GHz RF.	**Demonstrated at IBM Almaden Research Center (Rugar, Yannoni, and Sidles, 1992).**	The nuclear spin-lattice relaxation time is inconveniently long for MRFM experiments.
Cyclic inversion	Potentially feasible at cryogenic temperatures. Would require manipulation of single-domain magnetization.	**Theoretically feasible at low temperature, but not yet demonstrated. Easiest route to single-spin detection and imaging.**	**Demonstrated at IBM Almaden Research Center (Rugar et al., 1994).**
Spin precession	Potentially feasible for a mechanical oscillator matched to the ferromagnetic resonance frequency.	Potentially feasible, but ESR frequencies tend to be inconveniently high.	**Theoretically feasible, but not yet demonstrated. Useful for biological imaging applications, particularly if single-spin detection can be achieved (Sidles, Garbini, and Drobny 1992).**

possibility (Sidles, Garbini, and Drobny, 1992). Table I organizes these possibilities in a 3×3 grid.

This article focuses on the four boldface entries in Table I, particularly the detection of individual electron and nuclear magnetic moments. However, it is important to appreciate the potential applications of MRFM to the study of ferromagnetism, which are briefly discussed in Sec. IX.

A. SQUID-based detection of single electrons

Small magnetic signals are commonly detected by superconducting quantum interference devices (SQUIDs) (Jaklevic *et al.*, 1964; Clarke, 1990). Signal and noise levels in SQUIDs are reasonably well understood, and it is instructive to compare the predicted limits of SQUID sensitivity to those of MRFM.

We consider a thin film dc SQUID placed on a sample surface 50 Å above an isolated paramagnetic center (i.e., an unpaired electron) for the purpose of detecting the electron's magnetic moment (Fig. 9). We choose this device geometry because, as stated by Ketchen *et al.* (1989), "the most favorable arrangement for measuring a small magnetic moment is to have that moment positioned inside the inductive loop of a low noise dc SQUID."

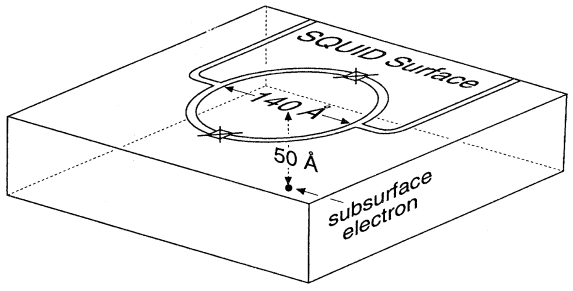

FIG. 9. SQUID loop coupled to a single electron located 50 Å below the loop.

For an electron with vertically oriented magnetic moment μ_B at a depth h_{depth}, the magnetic flux Φ captured by a surface-mounted pickup loop of radius r_{loop} is

$$\Phi = \mu_B \left(\frac{\mu_0}{2\pi}\right) \frac{\pi r_{\text{loop}}^2}{(r_{\text{loop}}^2 + h_{\text{depth}}^2)^{3/2}} , \tag{6.1}$$

with $\mu_0 = 4\pi \times 10^{-7}$ (SI units). The electron's magnetic moment is one Bohr magneton, $\mu_B = \hbar\gamma_e/2 = 9.27 \times 10^{-24}\,\text{J/T}$, in terms of Planck's constant $\hbar$ and the gyromagnetic ratio of the electron $\gamma_e/(2\pi) = 2.8\,\text{MHz/Gauss}$.

The loop radius can be optimized to capture the maximum flux signal; according to Eq. (6.1) the optimal radius is $r_{\text{loop}} = \sqrt{2}\,h_{\text{depth}}$. We therefore specify a pickup loop of radius 70 Å. The captured flux $\Phi = 2.2 \times 10^{-7}\,\Phi_0$, where Φ_0 is the flux quantum $\Phi_0 = \pi\hbar/e = 2.067 \times 10^{-15}\,\text{T m}^2$ and e is the electron charge.

This result is sobering as far as SQUID-based detection of single spins is concerned. The best available macroscopic SQUIDs achieve a flux sensitivity of approximately $10^{-7}\,\Phi_0/\sqrt{\text{Hz}}$ (Clarke, 1990). It would be an impressive technical feat to match this sensitivity using a pickup loop with radius 70 Å. Yet the loop cannot be made bigger without sacrificing signal strength, due to the $1/r_{\text{loop}}$ asymptotic dependence of Eq. (6.1).

Other engineering challenges become apparent when we calculate how much current must flow through the SQUID. Physical intuition suggests that detection of an interferometric phase $\delta\Phi/\Phi_0 \sim 2.2 \times 10^{-7}$ requires that at least $(\Phi_0/\delta\Phi)^2 \sim 2.1 \times 10^{13}$ electrons flow through the SQUID; otherwise shot noise will obscure the interferometric signal. This result is readily established for photon interferometry by the methods of Sec. IV.D, and we may reasonably expect that electron interferometers will behave similarly.

This expectation is supported by a detailed analysis of

dc SQUID noise presented by Tesche and Clarke (1977; see also Bruines, de Waal, and Mooj, 1982; de Waal, Schrÿner, and Llurba, 1984; Clarke, 1990). We assume the pickup loop consists of superconducting wire with radius $r_{\rm wire} = 20\,\text{Å}$, so the wire diameter is about 1/4 the SQUID loop diameter. Our results are only weakly sensitive to the size of the wire. The loop inductance $\mathcal{L}$ is approximately (Smythe, 1968)

$$\mathcal{L} \approx \mu_0\, r_{\rm loop} \ln\left(8\frac{r_{\rm loop}}{r_{\rm wire}}\right) = 3.6\times 10^{-14}\ \text{H}. \qquad (6.2)$$

Let I_0 be the critical current of the SQUID junctions. We assume the reduced inductance $\beta \equiv 2\mathcal{L}\, I_0/\Phi_0$ satisfies $\beta \ll 1$, and we check the consistency of this assumption later. Following Tesche and Clarke (1977), the SQUID is operated at a sufficiently low temperature that Johnson noise in the SQUID's shunt resistances is negligible, and at a current bias of twice the critical current.

Under these conditions, Eq. (29) of Tesche and Clarke's article (1977) yields (after some reorganization) a physically illuminating expression for the flux-noise spectral density S_Φ:

$$S_\Phi = 0.25\ \Phi_0^2\ \frac{e}{I_0} \quad [\text{SI units of } (\text{T m}^2)^2/\text{Hz}]. \qquad (6.3)$$

The coefficient 0.25 stems from numerical calculations. Note that S_Φ is independent of all SQUID device parameters except I_0.

According to Tesche and Clarke, Eq. (6.3) represents the quantum limit to the flux sensitivity of small-β dc SQUIDs. Subsequent work by Koch, Van Harlingen, and Clarke (1980, 1981a, 1981b) has shown that Eq. (6.3) was originally derived from an inappropriate model of shot noise in tunneling junctions, but nonetheless provides a reasonably accurate description of dc SQUID noise limits.[9]

[9]Tesche and Clarke's 1977 analysis leading to Eq. (6.3) was based on a theoretical model of shot noise by Stephen (1968) and an experiment by Dahm *et al.* (1969). Subsequently, Koch, Van Harlingen, and Clarke (1980, 1981a, 1981b) showed that the quantum noise limit in dc SQUIDs is not due to pair tunneling shot noise as originally assumed by Tesche and Clarke (because pair tunneling is reversible and hence noise-free), but instead originates in quantum zero-point fluctuations in junction shunt resistances. For an individual junction, the zero-point fluctuation voltage noise $S_V^{\rm fluct}$ of Koch, Van Harlingen, and Clarke is related to the voltage noise $S_V^{\rm shot}$ assumed by Tesche and Clarke by

$$S_V^{\rm fluct} = \left(\frac{R_d}{R}\right)^2 \left(\frac{I}{I_0}\right)^2 \frac{V}{I_0 R}\ S_V^{\rm shot}, \qquad (6.4)$$

with I the current bias, V the junction voltage, I_0 the junction critical current, R the shunt resistance, and $R_d = \partial V/\partial I$ the dynamic resistance. Present SQUID junctions are operated with $S_V^{\rm fluct} \sim S_V^{\rm shot}$ because (1) R_d is strictly greater than R for typical junction I-V curves, (2) biasing with $I \ll I_0$ and $V = 0$ is feasible, but results in zero SQUID flux sensitivity, and (3) biasing with $I \sim I_0$ and $V \ll I_0 R$ creates a compensating large dynamic resistance $R_d \gg R$, and also creates problems with junction stability. Thus Eq. (6.3) remains reasonably accurate for practical calculations.

To attain the desired single-electron flux sensitivity of $2.2\times 10^{-7}\Phi_0/\sqrt{\text{Hz}}$, SQUID junctions must support a critical current of at least $I_0 \approx 0.25\ (\Phi_0/\delta\Phi)^2\, e/\text{sec} = 0.85\,\mu\text{A}$. This implies that $\beta = 2.9\times 10^{-5}$, satisfying the condition $\beta \ll 1$ self-consistently.

Typically dc SQUIDs are biased at twice the critical current, so the required total current is $I_{\rm tot} = 2I_0 = 1/2\ (\Phi_0/\delta\Phi)^2\, e/\text{sec} = 1.7\,\mu\text{A}$, in reasonable agreement with our earlier simple estimate. Accordingly, the 20 Å radius SQUID loop wires must support a current density of order $2.7\times 10^7\,\text{A/cm}^2$, which approximates the maximum current density supported by present superconducting materials (Likharev, 1990; Edstam and Olsson, 1992). Enlarging the SQUID pickup loop does not greatly change the required current density, as the accompanying reduction in the flux signal necessitates larger critical currents, leaving the current density unchanged.

Attempting proton-moment detection is even more daunting. The intercepted flux is 650 times smaller, $\phi \approx 3.3\times 10^{-10}\phi_0$, requiring a critical current 650^2 times greater, $I_0 \approx 0.36$ A, and a current density of order $10^{13}\,\text{A/cm}^2$.

We see that dc SQUID detection of single-electron and proton magnetic moments requires submicron pickup loops in conjunction with large critical currents. These seemingly incompatible requirements might plausibly be reconciled by a suitable SQUID design. For example, proton detection might be achieved by coupling the proton's magnetic flux, via a submicron superconducting flux transformer loop, into a nearby much larger dc SQUID loop, capable of supporting the required Ampere-scale critical currents.

Ketchen *et al.* (1989) and Ketchen (1992) have reviewed design and fabrication issues associated with submicron dc SQUIDs, emphasizing their unique technical challenges. They calculate that a device with a minimum feature size of 0.5 μm might plausibly achieve single-μ_B sensitivity at 100 mK. Recently, Ketchen *et al.* (1993) have operated a SQUID susceptometer with an input loop diameter of 0.8 μm, achieving a magnetic-moment sensitivity of $\sim 100\,\mu_B/\sqrt{\text{Hz}}$ at 4.2 K. This is still 40 dB short of the signal-to-noise ratio required to detect a single-electron moment in a one-Hz bandwidth.

B. MRFM-based detection of single electrons

Now we will consider an MRFM design capable, in principle, of detecting individual electron moments at room temperature, with reasonably good signal-to-noise ratio. In doing so we will apply the results obtained earlier in this article, and illustrate how MRFM devices sidestep some of the difficulties that SQUIDs encounter.

1. The MRFM field source

MRFM technology resembles SQUID technology in that maximal sensitivity is achieved when the sample

magnetic moment is coupled to a submicron current source. However, the MRFM current source is ferromagnetic rather than superconducting.

We begin our MRFM design by affixing a single-domain ferromagnetic sphere to a cantilever (Sidles, Garbini, and Drobny, 1992; Kent *et al.*, 1993). The sphere acts as a dipole field source with magnetization axis oriented vertically, as shown in Fig. 10, generating a magnetic field gradient g:

$$g = 2\mu_0 M \frac{r_{\text{sphere}}^3}{(r_{\text{sphere}} + h_{\text{depth}})^4} . \tag{6.5}$$

We set $\mu_0 M = 2\,\text{Tesla}$, a magnetization typical of Fe and other strongly ferromagnetic materials. The sphere radius r_{sphere} is chosen to maximize the field gradient at a depth h_{depth} below the sample surface. Choosing $h_{\text{depth}} = 50\,\text{Å}$ as a desirable imaging depth, as in the previous SQUID design, the gradient is maximal when $r_{\text{sphere}} = 3h_{\text{depth}} = 150\,\text{Å}$.

An electron at a depth of 50 Å experiences a field gradient $g = 84\ \text{G/Å}$, which exerts a force F_{electron}

$$F_{\text{electron}} = g\hbar\gamma_e/2 = 7.8 \times 10^{-16}\,\text{N}. \tag{6.6}$$

This is comparable to the force sensitivity $F_{\text{min}} = 9 \times 10^{-16}\,\text{N}$ attained in the first MRFM experiment in a 0.1 Hz bandwidth (Rugar, Yannoni, and Sidles, 1992). Thus even the first MRFM experiment, in principle, could have achieved single-electron-moment sensitivity, if the device had been equipped with a sufficiently strong field gradient.

Physically, MRFM's sensitivity arises in part from the extraordinarily large effective current density of electron currents in the ferromagnet. Achieving the same magnetic moment with a superconducting current density j_{eff} oriented circumferentially within the sphere would require

$$j_{\text{eff}} = \frac{32}{3\pi}\frac{M}{r_{\text{sphere}}} = 3 \times 10^{10}\,\text{A/cm}^2, \tag{6.7}$$

corresponding to a net circulating current of 0.13 A.

Ferromagnetic currents are sustained without dissipation because ferromagnetism is a coherent quantum phenomenon, similar in many respects to superconductivity, but occurring at room temperature. At microscopic scales the effective ferromagnetic current density is substantially greater than present superconducting materials can support (Likharev, 1990).

2. Cantilever design and operation

Having coupled an electron moment to a strong ferromagnetic current, the next task is to couple the current to the macroscopic world. This is accomplished in two stages: first the ferromagnetic current is coupled to the cantilever motion in the simplest possible manner, by affixing the ferromagnetic sphere to the cantilever,[10] then the cantilever motion is monitored by an optical interferometer which generates a macroscopic position signal.

We specify a silicon nitride cantilever as described by Hoen *et al.* (1994): 55 μm long, 5 μm wide, and 200 Å thick, with density ρ of $3\,\text{gm/cm}^3$, modulus E of 140 GPa, and quality factor Q of 3000. The direction of the electron magnetic moment is sinusoidally modulated by cyclic adiabatic inversion, as in nuclear-spin MRFM experiments (Rugar *et al.*, 1994),[11] yielding a root-mean-square magnetic moment $\mu_B/\sqrt{2}$ and a root-mean-square force $g\mu_B/\sqrt{2}$. The ambient temperature is chosen to be 295 K, and the field source is the 300-Å-diameter Fe sphere described in the previous section.

These design parameters yield the following predicted operating parameters:

$$\begin{aligned} \text{cantilever motional mass} &= 4.1\ \text{pg}, \\ \text{spring constant} &= 8.6\ \mu\text{N/m}, \\ \text{resonant frequency} &= 7300\ \text{Hz}, \\ \text{damping time} &= 65\ \text{msec}, \end{aligned}$$

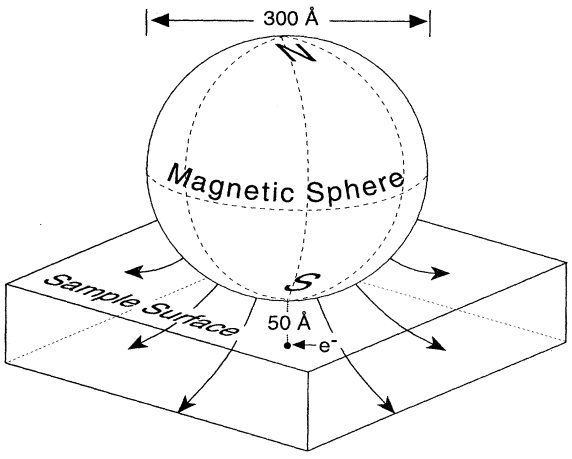

FIG. 10. A ferromagnetic gradient source.

[10] In existing MRFM experiments the sample is affixed to the cantilever and the gradient source is brought near; this inversion of source and sample position does not alter the fundamental physics.

[11] Cyclic inversion modulates the sample magnetization in an approximately, but not exactly, sinusoidal manner. The precise waveform of the time-dependent magnetization depends on details of the inversion method. The signal-to-noise ratios calculated in this article are not substantially affected thereby.

optimum optical power = 27 nW,
rms moment signal = 6.6×10^{-24} A m^2,
moment sensitivity = 3.8×10^{-25} A m$^2/\sqrt{\text{Hz}}$,
rms electron force signal = 5.5×10^{-16} N,
force sensitivity = 3.2×10^{-17} N$/\sqrt{\text{Hz}}$
single-electron SNR = 25 dB (in one Hz).

The theoretical sensitivity of this room-temperature MRFM design would allow force detection of an individual electron magnetic moment with a signal-to-noise ratio of 25 dB in a one-Hz bandwidth at room temperature.[12] At liquid-helium temperature, T=4.2 K, the force sensitivity improves to 3.8×10^{-18} N$/\sqrt{\text{Hz}}$ and the predicted signal-to-noise ratio improves from 25 to 43 dB, sufficient to detect individual electron moments with a signal-to-noise ratio of 13 dB in a bandwidth of 10^3 Hz.

Force detection thus could occur rapidly enough to allow scanning and imaging of samples containing many electron spins. The predicted cryogenic force sensitivity also suffices to detect the force from a single proton moment (1.2×10^{-18} N) with unity signal-to-noise ratio in a 0.1 Hz bandwidth.

Inversion of the electron-spin direction alters the effective spring constant of the cantilever by $\delta k = 2\mu_B \, \partial g/\partial z = 3.1 \times 10^{-7}$ N/m, altering the resonant frequency by $\delta\omega_0 = 130$ Hz. Cyclic inversion therefore modulates the cantilever resonant frequency with root-mean-square amplitude $130/(2\sqrt{2})$ Hz = 47 Hz.

The sensing methods of Albrecht *et al.* (1991) suffice to detect this FM signal. Assuming a 10-Å cantilever excitation amplitude, so that $\langle z^2 \rangle = 50$ Å^2 in Eqs. (4.12) and (4.13), the spring constant and frequency noise spectral densities at 295 K are

$$S_k^{1/2} = 4.5 \times 10^{-8} \, (\text{N/m})/\sqrt{\text{Hz}}, \tag{6.9}$$

$$S_\nu^{1/2} = 19 \, \text{Hz}/\sqrt{\text{Hz}}. \tag{6.10}$$

FM detection of a cyclically inverted single-electron moment thus yields a predicted signal-to-noise ratio of 7.8 dB in a one-Hz bandwidth at room temperature. Operation at 4.2 K improves the signal-to-noise ratio to 26 dB.

These relatively large signal-to-noise ratios suggest that a single-spin MRFM experiment has reasonable leeway to behave in nonideal fashion and still maintain an acceptable signal-to-noise ratio. This is important because (in our experience) MRFM experiments are not easy to accomplish, especially the first time; a surplus of predicted signal-to-noise ratio is therefore very welcome.

It is likely that MRFM cantilevers can be made smaller, colder, and with a longer damping time than the above example; this would further improve the magnetic-moment sensitivity.

[12]The signal-to-noise ratio (SNR) is defined to be

$$\text{SNR} = 10 \log_{10} \left| \frac{\text{signal power}}{\text{noise power}} \right| \text{ (in dB)}. \tag{6.8}$$

VII. MRFM AS A QUANTUM-LIMITED SENSING TECHNOLOGY

We have seen that MRFM comprises four physical mechanisms, which together form a linked chain connecting a quantum spin state to a macroscopic observer:

(1) The spin being observed is strongly coupled to a dissipation-free current density in a ferromagnetic source.
(2) The motion of the cantilever couples the ferromagnetic current to the fundamental cantilever mode, again in a dissipation-free manner.
(3) The fundamental cantilever mode is separated from higher modes by a frequency gap, isolating the fundamental mode from ambient thermal fluctuations.
(4) Optical interferometry provides quantum-limited sensing of the cantilever excitation.

In principle each link is nearly noise-free, making single-spin detection with MRFM a realistic possibility.

The only intrinsically dissipative link in this chain, and hence the only intrinsically noisy link, is the optical interferometer. But we have seen that a fiber-optic interferometer can approach quantum-limited sensitivity.

Cantilever damping is the other main dissipative mechanism in MRFM, but dissipation in mechanical oscillators has no known lower bound. Damping times of hours or longer are achievable in macroscale oscillators; it will be interesting to see whether microscale oscillators can achieve similarly long damping times.

VIII. STERN-GERLACH EFFECTS IN SINGLE-SPIN DETECTION

MRFM borrows from the original Stern-Gerlach experiment and its descendants (Ramsey, 1956; Wineland, Ekstrom, and Dehmelt, 1973; Brown and Gabrielse, 1986; Dehmelt, 1988, 1990; Bloom, 1993) the idea that small ensembles of particles are effectively self-polarizing.

Consider an ensemble of N individual spin-$\frac{1}{2}$ particles in a polarizing field, such that the mean polarization is $\langle p \rangle$. Ordinary statistical mechanics then implies the mean-square polarization $\langle p^2 \rangle$ is

$$\langle p^2 \rangle = \langle p \rangle^2 + (1 - \langle p \rangle^2)/N, \tag{8.1}$$

with the $1/N$ factor reflecting the contribution of statistical fluctuations to $\langle p^2 \rangle$.

In typical macroscopic experiments, $N \sim 10^{13}$ or greater, making fluctuations of $\langle p^2 \rangle$ negligible. In contrast, experiments detecting a single-spin ($N = 1$) measure $\langle p^2 \rangle = 1$ even in the absence of a polarizing field. The sign of the polarization is random in the limit $\langle p \rangle \to 0$.

Statistical mechanics thus predicts sufficiently small spin ensembles to be effectively self-polarizing. This effect is particularly important in MRFM detection of individual nuclear spins, which are difficult to polarize.

This simple statistical analysis agrees with a more rigorous quantum analysis, in which the quantum Hamiltonian of an MRFM device is specified, a complete set of eigenstates is constructed, and wave functions are evolved forward in time (Sidles, 1992; Sidles, Garbini, and Drobny, 1992). The self-polarization exhibited by MRFM devices is shown to be equivalent to the familiar Stern-Gerlach effect, as manifested in the cyclic phase space of the cantilever.

An analysis by Wootters and Zurek (1982) implies that Stern-Gerlach self-polarization will be observed by *any* device that measures the polarization of an individual spin state,[13] so it should be observed in cyclic adiabatic inversion experiments (Rugar *et al.*, 1994), as well as precession-resonant experiments (Sidles, 1992; Sidles, Garbini, and Drobny, 1992).

Dehmelt and collaborators (Wineland, Ekstrom, and Dehmelt, 1973; Brown and Gabrielse, 1986; Dehmelt, 1988, 1990) have experimentally demonstrated Stern-Gerlach self-polarization in geonium experiments, in which the oscillation frequency of a single trapped electron depends on the spin state. Consistent with the general arguments of Wootters and Zurek, isolated electrons are always measured to be either spin up or spin down; intermediate polarizations are never observed.

IX. MRFM APPLICATIONS IN MAGNETISM

A practical challenge of MRFM experiments lies in determining what is on the end of the cantilever. Suppose a 300-Å diameter Fe sphere of magnetization $\mu_0 M = 2$ Tesla is affixed to a cantilever, as illustrated in Fig. 11. How can we verify that the particle is present on the cantilever, and carries a magnetic moment suitable for MRFM imaging?

One diagnostic approach relies on the cantilever's torque sensitivity, as discussed in Sec. IV.C.2. An oscillating magnetic field of nominal amplitude 10 Gauss is applied to the particle, thus generating an oscillating torque of amplitude 2.25×10^{-20} N m. This torque excites the cantilever and generates a detectable signal. The room-temperature torque-noise spectral density of the 55-μm cantilever previously described is $S_J^{1/2} = 1.28 \times 10^{-21}\,\mathrm{N\,m}/\sqrt{\mathrm{Hz}}$, yielding a predicted signal-to-noise ratio of 22 dB in a one-Hz bandwidth.

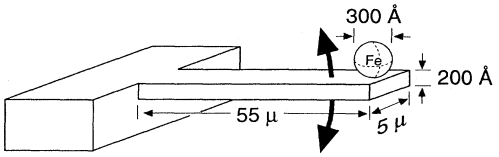

FIG. 11. A ferromagnetic sphere on a cantilever.

By varying the direction of the applied field and monitoring the resulting excitation of the cantilever, the magnitude and orientation of the particle's magnetic moment can be determined. Ferromagnetic resonance phenomena in the particle can be elicited by applying suitable rf fields.

Gibson and Schultz (1991) have performed a similar experiment, in which an 8-μm-Ni sphere was affixed to a force microscope cantilever, and the susceptibility of the particle measured as a function of an applied polarizing field. The cantilever was excited by an alternating magnetic-field gradient, which exerted an alternating force on the particle, rather than an alternating torque.

Room-temperature MRFM devices might thus observe a variety of magnetic phenomena in individual nanometer-scale single-domain magnetic particles. This capability is not surprising, if we reflect that an MRFM cantilever is effectively an ultra-low-mass vibrating sample magnetometer. No one has yet attempted an MRFM experiment involving single-domain magnetic particles, but this is a promising area for further research.

X. BIOMOLECULAR APPLICATIONS OF SINGLE-SPIN MRFM

It is standard laboratory practice to spin label proteins and DNA by attaching tempol and other compounds with unpaired electrons (Robinson *et al.*, 1985a, 1985b; Robinson, Haas, and Mailer, 1994). By spin labeling both a membrane-bound receptor and a protein that binds to it, the combined system might be directly imaged. Similarly, by spin labeling lipids within a bilayer, the lattice structure of the bilayer might be imaged, affording study of lipid diffusion. Some metalloproteins are naturally spin labeled, affording direct imaging by MRFM. Important metalloproteins include chlorophyll, hemoglobin, and nitrogenase.

More generally, the three-dimensional structure of any self-assembling protein/DNA/RNA complex might be studied by spin labeling its individual components, then using MRFM to image the assembled complex. Examples of such complexes include DNA, polymerase/DNA complexes, ribosomes, actin/integrin/membrane assemblies, the light harvesting complex, and viral architectures.

If MRFM imaging of single-electron moments is successful, we anticipate that it will serve as a bridge tech-

[13]Suppose that a hypothetical apparatus can nondestructively measure, as a continuous variable, the expectation value of the z component of spin, $\langle\Psi|\sigma_z|\Psi\rangle$. Here $|\Psi\rangle$ is an arbitrary spin state and σ_z is a Pauli matrix. By repeating this measurement along the x axis and y axis, enough information is obtained to "clone" the spin state (to within an overall phase). The reasoning of Wootters and Zurek may be readily extended to show that such cloning is incompatible with the linearity of quantum mechanics. Furthermore, Wootters and Zurek describe methods by which a measurement of $\langle\Psi|\sigma_z|\Psi\rangle$ alone can create causal paradoxes when applied to two entangled spin states separated by a spacelike interval.

nology leading to a more challenging, but more broadly applicable, technology for imaging individual nuclear magnetic moments. This would allow direct imaging of all biological molecules.

XI. CONCLUSION

The last two years have seen rapid experimental progress in MRFM. The design path to the detection of individual electron magnetic moments is reasonably clear. Up to the present time, both signal and noise in every MRFM experiment have been in reasonable accord with theoretical expectations. If this continues to be true of future experiments, then single-electron-moment detection will become practical in the next few years.

The applications of single-spin imaging are of sufficient practical importance, and the technical issues sufficiently well defined, to justify a serious and sustained development effort. However, it should be clearly understood that MRFM technology is in its early stages of development, and the limits of sensitivity cannot yet be foreseen.

Present research in MRFM emphasizes experiments that are doable and scalable. Here "doable" means that a working experiment can be built on a benchtop. "Scalable" means that making the apparatus smaller makes the experiment work better. This reflects our pragmatic opinion that progress is most likely to be achieved by cumulative improvement of working devices.

A key priority is the reduction of thermal noise to a level consistent with the detection of individual electrons and nuclei. Accordingly, over the next few years the most important MRFM research will be in the area of cantilever design, control, and noise. This research will provide a foundation for a wide range of applications in structural biology, solid state physics, material science, and polymer science.

ACKNOWLEDGMENTS

We acknowledge many helpful conversations with Frederick A. Matsen II, III, and IV, Tom Albrecht, Hans-Martin Vieth, Ray Kendrick, Koichi Wago, Roger Koch, Steve Ellis, Lowell Brown, David Thouless, Sam Fain, Cliff Slaughterbeck, Rob Van Dyck, Myer Bloom, Jurek Krzystek, Al Kwiram, Gary Drobny, Colin Mailer, Bruce Robinson, Bill Lytollis, and Rob Kaiser. Authors Sidles, Garbini, and Bruland gratefully acknowledge the support of the University of Washington Department of Orthopaedics, the NIH Biomedical Research Technology Program (BRTP) under R01 RR08820, and the NSF Instrument Development Program under BIR 9318002.

REFERENCES

Abragam, A., 1961, *Principles of Nuclear Magnetism* (Clarendon, Oxford), pp. 86 and 548.

Alberts, B., D. Bray, J. Lewis, M. Raff, K. Roberts, and J. D. Watson, 1994, *Molecular Biology of the Cell*, third edition (Garland, New York), pp. 148 and 155.

Albrecht, T. R., D. Grütter, D. Horne, and D. Rugar, 1991, J. Appl. Phys. **69**, 668–673.

Amrein, M., R. Durr, A. Stasiak, H. Gross, and G. Travaglini, 1989, Science **243**, 1708–1711.

Bartunik, H. D., L. J. Bartunik, and H. Viehmann, 1992, Philos. Trans. R. Soc. Lond. A **340**, 209–220.

Bernstein, F. C., T. F. Koetzle, G. J. B. Williams, E. F. Meyer Jr., M. D. Brice, J. R. Rodgers, O. Kennard, T. Shimanouchi, and M. Tasumi, 1977, J. Mol. Biol. **112**, 535–542.

Berry, B. S., and A. S. Nowick, 1966, in *Physical Acoustics Vol. IIIA*, edited by W. P. Mason (Academic, New York), pp. 1–42.

Binh, V. T., N. Garcia, and A. L. Levanuyk, 1994, Surf. Sci. Lett. **301**, L224–L228.

Binnig, G., H. Rohrer, C. Gerber, and E. Weibel, 1982a, Appl. Phys. Lett. **40**, 178–180.

Binnig, G., H. Rohrer, C. Gerber, and E. Weibel, 1982b, Phys. Rev. Lett. **49**, 57–60.

Binnig, G., H. Rohrer, C. Gerber, and E. Weibel, 1983, Phys. Rev. Lett. **50**, 120–123.

Binnig, G., C. F. Quate, and C. Gerber, 1986, Phys. Rev. Lett. **56**, 930–933.

Blair, D. G., 1991, in *The Detection of Gravitational Waves*, edited by D. G. Blair (Cambridge University Press, Cambridge, England), pp. 73–98.

Bloom, M., 1993, in *Nuclear Magnetic Double Resonance*, Proceedings of the International School of Physics "Enrico Fermi," edited by B. Maraviglia (North Holland, Amsterdam), pp. 473–484.

Brown, L. S., and G. Gabrielse, 1986, Rev. Mod. Phys. **58**, 233–312.

Bruines, J. J. P., V. J. de Waal, and J. E. Mooj, 1982, J. Low Temp. Phys. **46**, 383–396.

Buser, R. A., and N. F. de Rooij, 1990, Sens. Actuators A **21–23**, 323–327.

Caves, C. M., 1980, Phys. Rev. Lett. **45**, 75–79.

Caves, C. M., 1981, Phys. Rev. D **23**, 1693–1708.

Chen, G. Y., R. J. Warmack, T. Thundat, D. P. Allison, and A. Haug, 1994, Rev. Sci. Instrum. **65**, 2532–2537.

Cho, Y., S. Gorina, P. D. Jeffrey, and N. P. Pavletich, 1994, Science **265**, 346–355.

Clarke, J., 1990, in *Superconducting Devices*, edited by S. T. Ruggiero and D. A. Rudman (Academic, New York), pp. 51–101.

Clore, G. M., J. G. Omichinski, K. Sakaguchi, N. Zambrano, H. Sakamoto, E. Appella, and A. M. Groneborn, 1994, Science **265**, 386–391.

Cory, D. G., 1992, in *Annual Reports on NMR Spectroscopy*, edited by G. A. Webb (Academic, London), pp. 87–180.

Dahm, A. J., A. Denenstein, D. N. Langenberg, W. H. Parker, D. Rogovin, and D. J. Scalapino, 1969, Phys. Rev. Lett. **22**, 1416–1420.

Darnell, J. E., H. Lodish, and D. Baltimore, 1990, *Molecular Cell Biology*, third edition (Scientific American Books, New York).

Dehmelt, H., 1988, Z. Phys. D **10**, 127–134.

Dehmelt, H., 1990, Rev. Mod. Phys. **62**, 525–530.

de Waal, V. J., P. Schrijner, and R. Llurba, 1984, J. Low Temp. Phys. **54**, 215–232.

Drake, B., C. B. Prater, A. L. Weisenhorn, S. A. C. Gould, T. R. Albrecht, C. F. Quate, D. S. Cannell, H. G. Hansma,

and P. K. Hansma, 1989, Science **243**, 1586–1589.
Driscoll, R. J., M. G. Youngquist, and J. D. Baldeschwieler, 1990, Nature **346**, 294–296.
Edelstein, W. A., J. Hough, J. R. Pugh, and W. Martin, 1978, J. Phys. E **11**, 710–712.
Edstam, J., and H. K. Olsson, 1992, in *Superconducting Devices and Applications*, Springer Proceedings in Physics Vol. **64**, edited by H. Koch and H. Lübbig (Springer, Berlin), pp. 224–227.
Ferreirinho, J., 1991, in *The Detection of Gravitational Waves*, edited by D. G. Blair (Cambridge University, Cambridge), pp. 116–168.
Fraser, D. B., 1968, in *Physical Acoustics Vol. V*, edited by W. P. Mason (Academic, New York), pp. 59–110.
Friend, S., 1994, Science **265**, 334–335.
Garstens, M. A., and J. I. Kaplan, 1955, Phys. Rev. **99**, 459–463.
Gibson, G. A., and S. Schultz, 1991, J. Appl. Phys. **69**, 5880–5882.
Gould, S. A. C., B. Drake, C. B. Prater, A. L. Weisenhorn, S. Manne, G. L. Kelderman, H. J. Butt, H. Hansma, P. K. Hansma, S. Magonov, and H. J. Cantow, 1990, Ultramicroscopy **33**, 93–98.
Granato, A. V., and K. Lucke, 1966, in *Physical Acoustics Vol. IVA*, edited by W. P. Mason (Academic, New York), pp. 225–276.
Hansma, H. G., R. L. Sinsheimer, J. Groppe, T. C. Bruice, V. Elings, G. Gurley, M. Bezanilla, I. A. Mastrangelo, P. V. C. Hough, and P. K. Hansma, 1993, Scanning **15**, 296–299.
Hansma, H. G., A. L. Weisenhorn, S. A. C. Gould, R. L. Sinsheimer, H. E. Gaub, G. D. Stucky, C. M. Zaremba, and P. K. Hansma, 1991, J. Vac. Sci. Technol. B **9**, 1282–1284.
Harris, C. C., 1994, Science **262**, 1980–1981.
Hobbs, P., D. Abraham, and H. Wickramasinghe, 1989, Appl. Phys. Lett. **55**, 2357–2359.
Hoen, S., O. Züger, C. S. Yannoni, H. J. Mamin, K. Wago, and D. Rugar, 1994, in *Technical Digest of the 1994 Solid State Sensor and Actuator Workshop, Hilton Head, SC* (Transducers Research Foundation, Catalog No. 94TRF-0001), pp. 209–212.
Jaklevic, R. C., J. Lambe, A. H. Silver, and J. E. Mercereau, 1964, Phys. Rev. Lett. **12**, 159–160.
Kent, A. D., T. M. Shaw, S. von Molnar, and D. D. Awschalom, 1993, Science **262**, 1249–1252.
Ketchen, M. B., 1992, Springer Proceedings in Physics Vol. 64, edited by H. Koch and H. Lübbig (Springer, New York), pp. 256–264.
Ketchen, M. B., D. D. Awschalom, W. J. Gallagher, A. W. Kleinsasser, R. L. Sandstrom, J. R. Rozen, and B. Bumble, 1989, IEEE Trans. Magn. **25**, 1212–1215.
Ketchen, M., D. J. Pearson, K. Stawiasz, C. K. Hu, A. W. Kleinsasser, T. Brunner, C. Cabral, V. Chandrashekhar, M. Jaso, M. Manny, and K. Stein, 1993, IEEE Trans. Appl. Supercond. **3**, 1795–1799.
Klemens, P. G., 1966, in *Physical Acoustics Vol. IIIB*, edited by W. P. Mason (Academic, New York), pp. 201–234.
Koch, R. H., D. J. Van Harlingen, and J. Clarke, 1980, Phys. Rev. Lett. **45**, 2132–2135.
Koch, R. H., D. J. Van Harlingen, and J. Clarke, 1981a, Appl. Phys. Lett. **38**, 380–382.
Koch, R. H., D. J. Van Harlingen, and J. Clarke, 1981b, Phys. Rev. Lett. **47**, 1216–1219.
Lal, R., and S. A. John, 1993, Am. J. Physiol. **226**, C1–C21.
Langdon, R. M., and D. L. Dowe, 1987, Fiber Optic Sensors II, SPIE **798**, 86–93.
Lauterbur, P. C., 1973, Nature **242**, 190–191.
Likharev, K. K., 1990, in *Superconducting Devices*, edited by S. T. Ruggiero and D. A. Rudman (Academic, New York), pp. 1–50.
Mamin, H. J., D. Rugar, J. E. Stern, R. E. Fontana Jr., and P. Kasiraj, 1989, Appl. Phys. Lett. **55**, 318–320.
Mansfield, P., and P. G. Morris, 1982, *NMR Imaging in Biomedicine* (Academic, New York).
Martin, Y., and H. K. Wickramasinghe, 1987, Appl. Phys. Lett. **50**, 1455–1457.
Mason, W. P., 1942, *Electromechanical Transducers and Wave Filters* (Van Nostrand, New York), p. 90.
Mason, W. P., 1966, in *Physical Acoustics Vol. IIIB*, edited by W. P. Mason (Academic, New York), pp. 235–286.
Mastrangelo, I. A., M. Bezanilla, P. K. Hansma, P. V. C. Hough, and H. G. Hansma, 1994, Biophys. J. **66**, 293–296.
Morrow, C. D., J. Part, and J. K. Wakefield, 1994, Am. J. Physiol. **266**, C1135–C1156.
Morse, P. M., 1936, *Vibration and Sound* (McGraw-Hill, New York), pp. 119–120.
Neumeister, J. M., and W. A. Ducker, 1994, Rev. Sci. Instrum. **65**, 2527–2531.
Pace, A. F., M. J. Collett, and D. F. Walls, 1993, Phys. Rev. A **47**, 3173–3189.
Pitcher, R. J., K. W. H. Foulds, J. A. Clements, and J. M. Naden, 1990, Sens. Actuators A **21–23**, 387–390.
Ramsey, N., 1956, *Molecular Beams* (Clarendon, Oxford).
Randall, R. H., F. C. Rose, and C. Zener, 1939, Phys. Rev. **56**, 343–348.
Rees, W. A., R. W. Keller, J. P. Vesenka, G. Yang, and C. Bustamante, 1993, Science **260**, 1646–1649.
Roberts, R. L., R. G. Kessel, and H. Tung, 1991, *Freeze Fracture Images of Cells and Tissues* (Oxford University, Oxford).
Robinson, B. H., D. A. Haas, and C. Mailer, 1994, Science **263**, 490–493.
Robinson, B., H. Thomann, A. H. Beth, P. Fajer, and L. Dalton, 1985a, in *EPR and Advanced EPR Studies of Biological Systems*, edited by L. R. Dalton (CRC, Boca Raton), pp. 12–108.
Robinson, B., H. Thomann, A. H. Beth, P. Fajer, and L. Dalton, 1985b, in *EPR and Advanced EPR Studies of Biological Systems*, edited by L. R. Dalton (CRC, Boca Raton), pp. 296–301.
Roszhart, T. V., 1990, in *IEEE Sensor and Actuator Workshop* (IEEE, Hilton Head Island, SC), pp. 13–16.
Rugar, D., and P. Grütter, 1991, Phys. Rev. Lett. **67**, 699–702.
Rugar, D., and P. Hansma, 1990, Physics Today **43** (October), 23–30.
Rugar, D., H. J. Mamin, and P. Guethner, 1989, Appl. Phys. Lett. **55**, 2588–2590.
Rugar, D., C. S. Yannoni, and J. A. Sidles, 1992, Nature **360**, 563–566.
Rugar, D., O. Züger, S. Hoen, C. S. Yannoni, H. M. Vieth, and R. D. Kendrick, 1994, Science **264**, 1560–1563.
Sáenz, J. J., N. Garcia, P. Grütter, E. Meyer, H. Heinzelmann, R. Weisendanger, L. Rosenthaler, H. R. Hidber, and H. J. Gütherodt, 1987, J. Appl. Phys. **62**, 4293–4295.
Sidles, J. A., 1991, Appl. Phys. Lett. **58**, 2854–2856.
Sidles, J. A., 1992, Phys. Rev. Lett. **68**, 1124–1127.
Sidles, J. A., J. L. Garbini, and G. P. Drobny, 1992, Rev. Sci. Instrum. **63**, 3881–3899.

Sidles, J. A., and D. Rugar, 1993, Phys. Rev. Lett. **70**, 3506–3509.
Slichter, C. P., 1989, *Principles of Magnetic Resonance*, third edition (Springer, New York).
Smythe, W. R., 1968, *Static and Dynamic Electricity*, third edition (McGraw-Hill, New York), pp. 339–340.
Stephen, M. J., 1968, Phys. Rev. Lett. **21**, 1629–1632.
Stuart, D., 1994, Nature **371**, 19.
Tesche, C. D., and J. Clarke, 1977, J. Low Temp. Phys. **29**, 301–331.
Weisenhorn, A. L., B. Drake, C. B. Prater, S. A. C. Gould, P. K. Hansma, F. Ohnesorge, M. Egger, S. P. Heyn, and H. E. Gaub, 1990, Biophys. J. **58**, 1251–1258.
Whitfield, G., and A. G. Redfield, 1957, Phys. Rev. **106**, 918–920.
Wilson, J., and T. Hunt, 1994, *Molecular Biology of the Cell: The Problems Book* (Garland, New York).
Wineland, D. J., P. Ekstrom, and H. G. Dehmelt, 1973, Phys. Rev. Lett. **31**, 1279–1282.
Wootters, W. K., and W. H. Zurek, 1982, Nature **299**, 802–803.
Yannoni, C. S., O. Züger, J. A. Sidles, and D. Rugar, 1994, in *Encyclopedia for Magnetic Resonance*, edited by D. M. Grant and R. K. Harris (John Wiley and Sons Ltd., Sussex), in press.
Youngquist, M. G., R. J. Driscoll, T. R. Coley, W. A. Goddard, and J. D. Baldeschwieler, 1991, J. Vac. Sci. Technol. B **9**, 1304–1308.
Zener, C., 1937, Phys. Rev. **52**, 230–235.
Zener, C., 1938, Phys. Rev. **53**, 90–99.
Zhang, L. M., D. Uttamchandani, and B. Culshaw, 1990, Sens. Actuators A **21–23**, 391–393.
Zook, J. D., D. W. Burns, H. Guckel, J. J. Sniegowski, R. L. Engelstad, and Z. Feng, 1992, Sens. Actuators A **35**, 51–59.
Züger, O., and D. Rugar, 1993, Appl. Phys. Lett. **63**, 2496–2498.
Züger, O., and D. Rugar, 1994, J. Appl. Phys. **75**, 6211–6216.

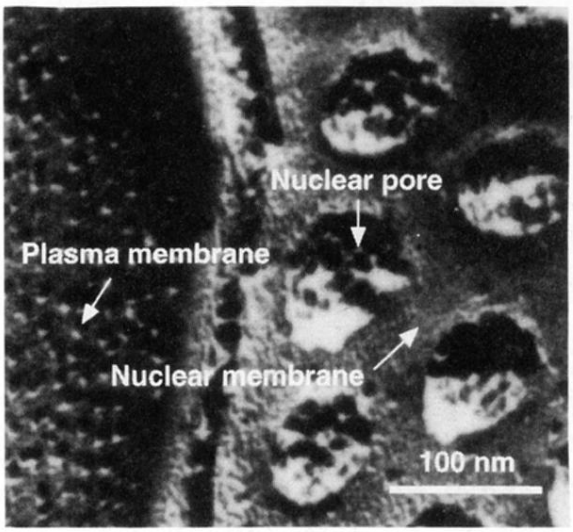

FIG. 1. Electron microscope image of a mouse sperm cell. The larger "domes" are nuclear pore structures embedded in the nuclear membrane. Tightly packed nanometer-scale particles in the plasma membrane also are featured. The detailed molecular structure of these features is unknown, and cannot readily be determined by any existing technology.

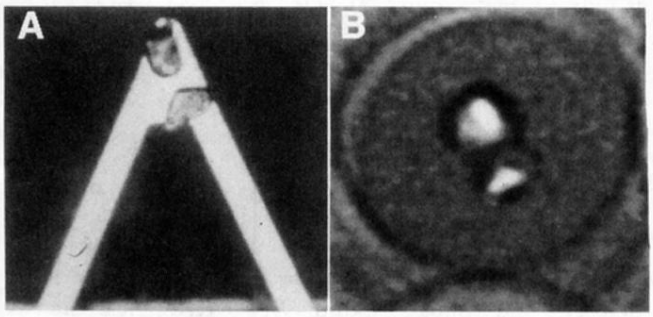

FIG. 4. Imaging by MRFM. (a) Optical micrograph showing two DPPH particles (20 μm wide) attached to a silicon nitride cantilever. (b) The reconstructed image, with the two DPPH particles appearing as two bright features. The large rings slightly visible in the image are artifacts of the deconvolution procedure (from Züger and Rugar, 1994).

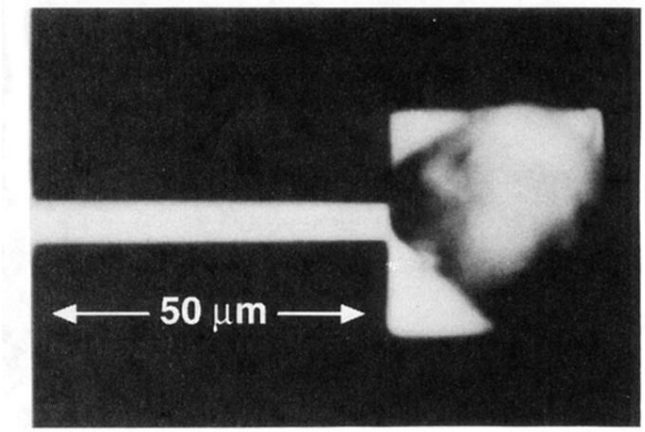

FIG. 6. Optical micrograph of a 900-Å thick silicon nitride cantilever. A small grain of the sample material (ammonium nitrate) is visible on the upper portion of the paddle-shaped cantilever tip. The narrow neck of the cantilever is 50 μm long and 5 μm wide (from Rugar *et al.*, 1994).